



Morphological change within and around a rectangular array of emergent vegetation is linked to flow structure

Yuan-Heng Zhang^{1,2}  and Heidi Nepf¹ 

¹Department of Civil and Environmental Engineering, Massachusetts Institute of Technology, Cambridge, MA, USA

²Department of Civil and Environmental Engineering, The Hong Kong Polytechnic University, Hong Kong SAR 999077, PR China

Corresponding author: Yuan-Heng Zhang, akiyh@mit.edu

(Received 10 March 2025; revised 21 May 2025; accepted 14 July 2025)

This study connected flow structure and morphological changes in and around a rectangular vegetation patch. The emergent patch was constructed in an 8 cm sand bed. Two patch densities were tested, using a regular configuration of rigid dowels. Near the leading edge of the patch, enhanced turbulence levels produced sediment erosion. Some of the eroded sediment was carried into the patch, forming an interior deposition dune. The denser patch resulted in a smaller dune due to stronger lateral flow diversion and weaker interior streamwise velocity. After the leading-edge dune, in the fully developed region of the patch, vortices formed in the shear layers along the patch lateral edges. Elevated turbulence at the patch edge produced local erosion. For the dense patch, material eroded from the edge was transported into the patch to form a flow-parallel ridge, and there was no net sediment loss/gain by the patch. For the sparse patch, material eroded from the edge was transported away from the patch, resulting in a net loss of sediment from the patch. In the wake of both patches, deposition occurred near the wake edges and not at the wake centreline, which was attributed to the weak lateral transport associated with the weakness of the von Kármán vortex street. Specifically, the lateral transport length scale was less than half the width of the patch. The increasing bedform height within the wake progressively weakened and narrowed the von Kármán vortex street, illustrating an important feedback from morphological evolution to the flow structure. Despite significant local sediment redistribution, the patch did not induce channel-scale sediment transport.

Key words: sediment transport, shear layers, vortex streets

1. Introduction

Aquatic vegetation is a critical component in coastal and riverine ecosystems, forming important wetland and littoral habitat. Vegetation is particularly noted for retaining sediment and maintaining bed stability in coastal and riverine ecosystems (e.g. Orth *et al.* 2020; Temmink *et al.* 2022; Xu *et al.* 2022). Vegetation introduces additional resistance (James *et al.* 2004; Aberle & Järvelä 2013), which reduces velocity (Liu *et al.* 2020). This tends to enhance sediment deposition and retention of sediment (Bouma *et al.* 2007; Follett & Nepf 2012), which can promote the growth of ridges and islands (Larsen & Harvey 2010; Gu *et al.* 2019). However, vegetation also generates turbulence (Tanino & Nepf 2008; Yager & Schmeeckle 2013), facilitating sediment resuspension (Tinoco & Coco 2016; Yang, Chung & Nepf 2016), leading to erosion and reduction of bed elevation (Norris *et al.* 2021). Changes to the bedform can in turn affect the flow dynamics (Colombini & Stocchino 2012) and the continued growth of aquatic plants (Gurnell 2014). These feedback mechanisms complicate predictions of how vegetation distribution impacts sediment retention and river morphology. Unfortunately, during past decades, vegetation has been removed or lost from rivers, deltas (Nittrouer *et al.* 2012; Minderhoud *et al.* 2019) and lakes (Zhang *et al.* 2017), due to natural causes and agricultural and industrial land use (Coleman, Huh & Braud 2008; Elsey-Quirk *et al.* 2024). To restore and manage aquatic vegetation ecosystems, it is necessary to understand the interaction between flow, vegetation and sediment motion (Paola *et al.* 2011; Fagherazzi, Bryan & Nardin 2017).

Several previous studies have investigated the impact of an emergent vegetation patch of finite length and width on flow structure, sediment transport and bed morphological changes. Flow approaching a finite vegetation patch is diverted laterally away from the patch, causing flow acceleration along the vegetation edge (figure 1), which can generate erosion (Rominger, Lightbody & Nepf 2010). Flow that enters the patch will decelerate over a distance termed the interior adjustment length (L_i in figure 1), which decreases with increasing patch density (Rominger & Nepf 2011; Chen, Chan & Li 2012). Scour often occurs at the leading edge, with scoured material deposited farther downstream within the patch (e.g. Le Bouteiller & Venditti 2014). The region of scour in the patch is limited to the interior adjustment length, which increases with decreasing patch density, such that the scour and deposition within the patch also increase with a decreasing vegetation density (Kim *et al.* 2015a). Downstream of the interior adjustment length, vortices form along the flow-parallel interface from the Kelvin–Helmholtz (KH) instability (figure 1; Rominger & Nepf 2011). The KH structures can contribute to the lateral transport of sediment between the vegetated region and the open channel through two mechanisms: by enhancing the turbulent diffusion of sediment across the interface and by inducing a wave oscillation in the flow field within the patch (Zong & Nepf 2011).

Inside a vegetation patch, vegetation-generated turbulence has been shown to be a more important control than bed shear stress on the initiation of sediment motion and rates of sediment transport (Tinoco & Coco 2016; Yang *et al.* 2016; Yang & Nepf 2018). Because vegetation-generated turbulence can augment erosion and sediment transport, deposition within the patch is only favoured when the velocity is reduced sufficiently to eliminate vegetation-generated turbulence (Liu & Nepf 2016). Even if the velocity is reduced sufficiently within the patch to favour deposition and sediment retention, the accumulation of sediment inside the patch may still be limited by sediment supply into the patch (e.g. Zong & Nepf 2011; Xu *et al.* 2022). Sediment accumulation within a patch also depends on the sediment mobility within the channel. For channel velocity below the sediment motion threshold, erosion occurs adjacent to the patch and near the leading edge of the patch, as described above, but for channel velocity above the sediment

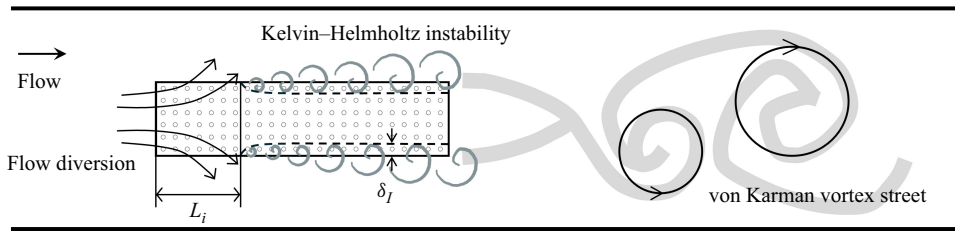


Figure 1. Top view of an emergent vegetation patch within a channel, illustrating the flow structures formed inside and in the wake of the patch. At the leading edge of the patch, the flow decelerates and is diverted laterally out of the patch over the interior adjustment length L_i . Shear layers form along each flow-parallel edge, which produce vortices by KH instability. These vortices, and the associated enhanced momentum exchange (Reynolds stress), penetrate a distance δ_l into the patch. A von Kármán vortex street may form in the wake of the patch.

motion threshold, sediment accumulation within and around the patch can occur (Kim *et al.* 2015a).

The flow evolution and morphological response downstream of the patch can influence the streamwise expansion of the patch (e.g. Gurnell 2014; Kondziolka & Nepf 2014). Downstream of the patch, the interaction between the lateral shear layer on either side of the patch can lead to the formation of a von Kármán vortex street (Zong & Nepf 2012). Follett & Nepf (2012) investigated sediment patterns related to an emergent circular patch under flow conditions that were above the sediment motion threshold. For a high-flow-blockage patch, the von Kármán vortex street in the patch wake directs deposition to the centreline of the wake. However, for a low-flow-blockage patch, the von Kármán vortex street is weak or absent, and deposition does not occur on the wake centreline, but, instead, deposits along the sides of the wake creating a bedform that is open to the downstream direction. These bed morphological changes will, in turn, alter the flow structure (Kirkil, Constantinescu & Ettema 2008; Kirkil & Constantinescu 2010; Chang, Constantinescu & Tsai 2017; Narayana, Timbadiya & Patel 2022). For instance, the bed deformation within a patch of model vegetation tends to shorten the interior adjustment length and reduce bed shear stress and vorticity arising from coherent vortices along the side edge of an array (Yi *et al.* 2021). Similarly, when scour around a circular cylinder produces a deposition mound in the cylinder wake, the upwelling flow associated with the mound can interfere with the formation of the von Kármán vortex street, making it weaker and less coherent (Kirkil, Constantinescu & Ettema 2009).

Along coasts, artificial structures such as brushwood dams and bamboo arrays are used to enhance sediment deposition and retention (Siemes *et al.* 2020; Siegersma *et al.* 2023) for the purpose of increasing bed elevation and facilitating vegetation colonisation. In addition, these porous structures dissipate wave energy (Bouma *et al.* 2016), mitigating erosion of a marsh fringe due to storms and waves (Townend *et al.* 2011). The enhanced marsh accretion and protection from erosion improves the resilience of coastal ecosystems. While previous studies have described some aspects of flow and turbulence within and adjacent to porous, emergent structures, such as brushwood dams (e.g. figure 1), many aspects of patch-flow-morphology feedback still require investigation to enable prediction of sediment loss and accretion from finite patches of emergent vegetation and porous structures designed to mitigate erosion. The present study considered the morphological response to an in-stream rectangular patch of emergent cylinders, focusing on the role of vortices formed along the patch flow-parallel edges and in the wake as agents of sediment transport.

b (cm)	Φ	N (m^{-2})	a (m^{-1})	L_i (m)	$L_{i,c}$ (m)	L_s (m)	L_d (m)	h_s (cm)	h_d (cm)	V_e (cm^3)	V_d (cm^3)
19.7	19.6 %	1550	19.7	0.9	1.4 (0.1)	0.20 (0.1)	0.36 (0.1)	-2.8 (0.1)	1.6 (0.1)	1150 (110)	270 (30)
18.3	4.9 %	388	4.9	—	2.2 (0.2)	0.39 (0.1)	0.56 (0.1)	-6.3 (0.1)	4.5 (0.1)	3240 (30)	1780 (20)

Table 1. Summary of experimental parameters. Values in parentheses indicate uncertainty. L_i is the measured interior adjustment length; $L_{i,c}$ is the calculated interior adjustment length, (3.1); L_s is the length of the scour region measured from the patch leading edge; h_s is the depth of the scour; L_d and h_d are the length and height of the depositional dune within the patch; V_e is the volume of erosion at the leading edge of the patch; and V_d is the volume of the deposition mound inside the patch.

2. Methods

Laboratory experiments were conducted in a 1 m wide and 10.4 m long channel, with water and sediment recirculated separately. Individual patches of model emergent vegetation were placed symmetrically on the channel centreline. The model vegetation consisted of circular wooden dowels with a diameter $d = 1.27$ cm, which were held in a regular pattern by perforated PVC baseboards. The dowels extended through the entire water depth. Upstream of the patch, the streamwise velocity was laterally uniform (figure S1 of the supplementary material available at [https://doi.org/10.1017/jfm.2025.10492]). The experiments were designed to compare the morphological response to a dense patch, for which sediment supply may be limited in the interior of the patch, with the response to a sparse patch, for which KH vortices were expected to penetrate the patch and provide supply into the patch. To achieve this comparison, the patch geometry was chosen based on the non-dimensional flow blockage C_{Dab} greater and less than 2, as defined in Rominger & Nepf (2011). Specifically, $C_{Dab} = 0.91$ and $C_{Dab} = 3.88$ were chosen to represent low and high flow blockage, respectively. Here C_D is the drag coefficient of the array elements, $C_D = 1$ was assumed for simplicity (Rominger & Nepf 2011), a ($= 4.9$ and 19.7 m^{-1}) is the frontal area per volume within the array and b ($= 18.3$ and 19.7 cm) is the half-width of the array. The corresponding solid volume fraction ($\Phi = N\pi d^2/4$, in which N (m^{-2}) is the number of dowels per unit bed area) was 4.9 % for the low-flow-blockage array and 19.6 % for the high-flow-blockage array. The array length was set to $L = 2.65$ m based on preliminary tests to ensure the full development of KH vortices. The array parameters are summarised in table 1. After the patch was installed, an 8 cm layer of sand ($d_{50} = 0.35$ mm, $\rho_s = 2650 \text{ kg m}^{-3}$) was placed over the entire 10.4 m test section and manually flattened.

The water depth was $h = 20$ cm above the top of the initially flat sand layer, measured with a ruler upstream of the array. The mean water surface had negligible (< 5 mm) variation along the flume length. The incoming (and channel average) velocity was $U_o = 16.0 \pm 0.8 \text{ cm s}^{-1}$. The channel Froude and Reynolds numbers were $Fr_h = U_o/\sqrt{gh} = 0.11$ and $Re_h = U_o h/\nu = 32\,000$, respectively, in which ν ($= 10^{-6} \text{ m}^2 \text{ s}^{-1}$) is the water kinematic viscosity and g is gravity. The Froude and Reynolds numbers indicated that the flow was subcritical and fully turbulent. The bed friction coefficient C_f representing both grain resistance and the bedform drag, when present, was estimated as

$$C_f = \frac{1}{8} \left(0.32 \left(\frac{d_{50}}{h} \right)^{\frac{1}{3}} + \frac{\Delta}{\Lambda} \right), \quad (2.1)$$

in which Δ is the dune height and Λ is the dune length (equations (8.18b) and (8.21) in Julien (2010)). For the initial flat bed, $C_f = (1/8)(0.32(d_{50}/h)^{1/3}) = 0.005$. The dimensionless particle diameter $d_* = d_{50}[(\rho_s - \rho)g/\rho v^2]^{1/3} = 8.85$. For $0.3 < d_* < 19$, the critical Shields parameter $\tau_{*c} = 0.25d_*^{-0.6} \tan 30^\circ = 0.039$ (Julien 2010), indicating a critical shear velocity of $u_{*c} = \sqrt{((\rho_s - \rho)g/\rho)d_{50}\tau_{*c}} = 0.015 \text{ m s}^{-1}$. The incoming velocity was lower than the critical velocity required for the sediment motion, $U_o < U_c = u_{*c}/\sqrt{C_f} = 0.22 \text{ m s}^{-1}$. Consistent with this, no sediment motion was observed in the region upstream of the array. The critical bed shear stress $\tau_c = \tau_{*c}(\rho_s - \rho)gd_{50} = 0.22 \text{ Pa}$ was used to infer a critical level of turbulent kinetic energy for sediment motion, $k_{t,c} = \tau_c/0.19\rho = 1.2 \times 10^{-3} \text{ m}^2 \text{ s}^{-2}$ (e.g. Yang *et al.* 2016).

Velocity was measured by a 3D Nortek Vectrino acoustic Doppler velocimeter (ADV), with a sampling time of 120 s and a sampling rate of 200 Hz. The necessary sampling duration was confirmed by a convergence test (figure S2 of the supplementary material) of mean and turbulent flow statistics. Spherical glass beads (Potters Industries Inc. 110P8, median grain size $d_{50} = 10 \text{ }\mu\text{m}$) were added to improve the backscatter signal. For each sampling point within the array, the ADV was placed as close as possible to the midpoint between four dowels. The velocity at this position was confirmed to be within 11 % of the spatially averaged velocity measured by five positions within a unit cell, including four corners and the midpoint (see figure S3 of the supplementary material). Velocity measurements were made at several times after the start of the experiment to observe how the evolution of the bed influenced the velocity field. Once the velocity became steady with time, we considered the bedform to be fully developed, though some ripple migration continued to be observed.

Based on vertical profiles measured in this study (figure S4 of the supplementary material) and previous studies (Shan *et al.* 2020; Zhao & Nepf 2021), for emergent arrays of cylinders, the velocity measured at mid-depth can reasonably represent the depth-averaged velocity, and the flow can be considered approximately two-dimensional. The origin of the Cartesian coordinate system ($x = 0$, $y = 0$) was placed at the leading edge of the array and at the mid-point of the array and channel, respectively, with x positive in the streamwise direction (figure 2). The velocity components were denoted as (u, v) in the (x, y) directions, respectively. Velocity was collected along the channel centreline, along the flow-parallel edge of the array and along multiple lateral transects within and downstream of the array (red dashed lines in figure 2). The flow structure and morphological changes were mostly symmetric across the centreline of the array and channel, which was confirmed by the measurements across the whole flume width (figure S5 of the supplementary material). Subsequently, to reduce measurement time, the remaining lateral transects were collected over half of the flume width (figure 2). The bed elevation was measured with a vertical resolution of $\pm 1 \text{ mm}$ before and after exposure to a fixed duration of flow using a down-looking Nortek Vectrino. The change in bed elevation before and after exposure to flow is defined as the net deposition, δ_b . The length of the scour region measured from the patch leading edge is defined as the scour length, L_s . The length of the depositional dune measured from the end of the scour region $x = L_s$ is referred to as L_d . By integrating the net deposition δ_b across the scour region ($x = 0$ to L_s) within the patch ($y = 0$ to b), the volume of erosion at the leading edge of the patch is $V_e = \int_0^{L_s} \int_0^b \delta_b \text{ dy dx}$. The volume of the deposition mound inside the patch was quantified by integrating the net deposition δ_b from $x = L_s$ to $L_s + L_d$ and from $y = 0$ to b , i.e. $V_d = \int_{L_s}^{L_s+L_d} \int_0^b \delta_b \text{ dy dx}$. Using the water surface as reference, the local water depth was defined as the difference between the water surface and local bed elevation.

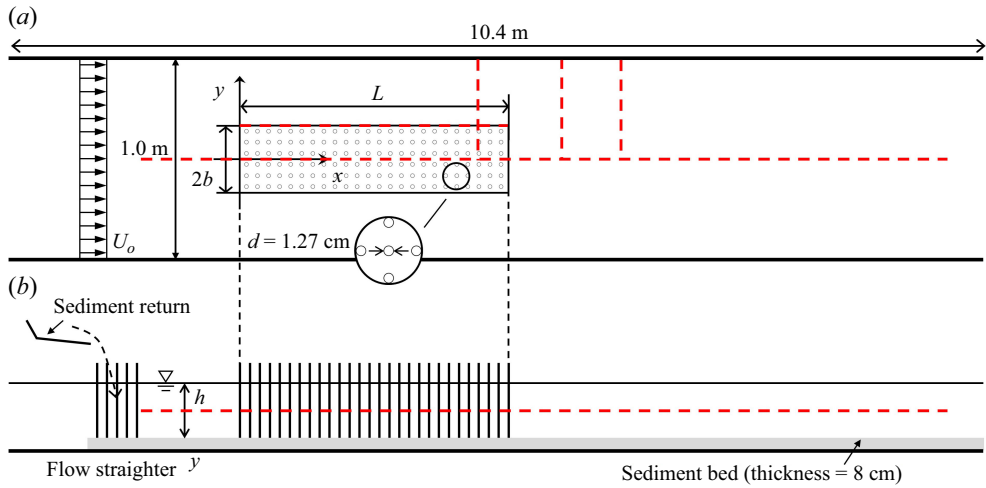


Figure 2. Experiment set-up. (a) Top view. (b) Side view. Not to scale. The longitudinal and transverse coordinates and velocity are (x, y) and (u, v) , respectively. Red dashed lines indicate measurement transects, including the centreline, the flow-parallel edge and several lateral cross-sections.

The raw velocity data were prefiltered by removing data with a correlation coefficient less than 70 %. The spikes in velocity records were removed by the method developed by Goring & Nikora (2002). Each velocity record was decomposed into time-averaged (\bar{u}, \bar{v}) and fluctuating (u', v') components. The magnitude and spatial evolution of turbulent structures were evaluated using the power spectral density (PSD) of the cross-stream velocity (v), and with lateral and streamwise profiles of Reynolds stress, $-\overline{u'v'}$, turbulent kinetic energy $k_t = 1/2(\overline{u'^2} + \overline{v'^2})$, and root-mean-square velocity fluctuation, $u_{rms} = \sqrt{\overline{u'^2}}$, $v_{rms} = \sqrt{\overline{v'^2}}$. The PSD was estimated by Welch's method (Welch 1967), as described in the MATLAB toolbox. Peaks in the PSD indicated the presence of coherent vortices and their dominant frequency. The lateral profiles of velocity were used to estimate the momentum thickness of the shear layer (θ) and the expected dimensionless frequency of the KH instability, $f_{KH}\theta/\bar{U} = 0.032$ (Ho & Huerre 1984), in which $\bar{U} = 1/2(U_1 + U_2)$ and $\theta = \int_{-\infty}^{\infty} [(1/4) - ((\bar{u}(y) - \bar{U})/\Delta U)^2] dy$. Here U_1 and U_2 are the lowest velocity within the array and highest velocity adjacent to the array, respectively, and $\Delta U = U_2 - U_1$. The von Kármán vortex formed in the wake of the array was expected to have frequency f_{VK} in agreement with Strouhal number $2f_{VK}b/U_2 = 0.2$, based on a previous study of circular patch wakes (Zong & Nepf 2012).

Flow visualisation was used to examine the vortex structures in the wake. Red dye was injected with constant flow rate at both corners of the trailing edge of the patch. A camera was placed above and downstream of the test section, capturing the region downstream of the patch. Pictures were post-processed using Photoshop software to enhance the colour of the dye. The vortex frequency was extracted from the videos. The frequency extracted from the video was consistent with the dominant frequency in the PSD (figure S6 of the supplementary material).

3. Results

The change in the velocity field and introduction of new turbulence structures in response to the rectangular patch are discussed first, and these changes in the flow field are related

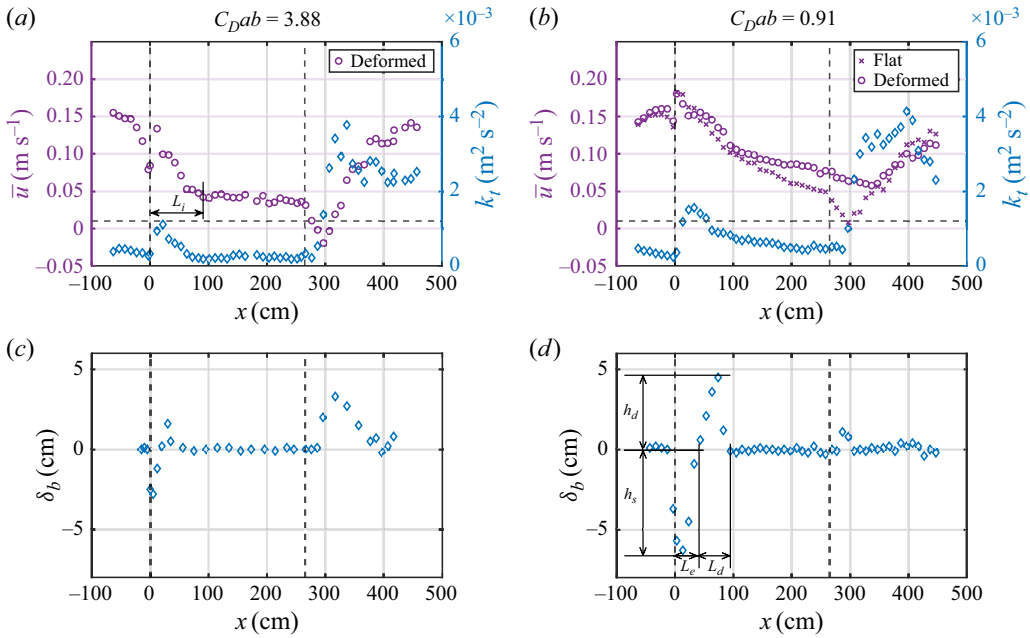


Figure 3. Longitudinal profiles of (a,b) time-averaged streamwise velocity (\bar{u}) and turbulent kinetic energy (k_t) and (c,d) net deposition (δ_b) for (a,c) high-flow-blockage patch and (b,d) low-flow-blockage patch. The data were collected on the centreline ($y = 0$). Vertical dashed lines indicate the leading ($x = 0$) and trailing ($x = L$) edges of the array. In (a,b), the horizontal dashed line indicates the estimated critical turbulence level for sediment mobility.

to morphological changes. After this, the feedback from morphological changes to the velocity structure is analysed.

3.1. Velocity and bedform evolution through the patch

Starting at the leading edge ($x = 0$), velocity within the patch decelerated over the interior adjustment length, L_i , and then reached a nearly constant value (figure 3a,b). Theory and scaling over a flat bed predict (Rominger & Nepf 2011)

$$L_{i,c} = \begin{cases} (3.0 \pm 0.3) \left[\frac{2}{C_{Da}} (1 + (C_{Dab})^2) \right], & C_{Dab} < 2 \\ (7.0 \pm 0.4)b, & C_{Dab} \geq 2. \end{cases} \quad (3.1)$$

However, in this study, the bed did not remain flat. In particular, significant scour and deposition occurred near the leading edge (figure 3c,d). The presence of bedforms shortened the adjustment length, relative to (3.1). Specifically, for the high-flow-blockage patch, $C_{Dab} = 3.88$, (3.1) predicted $L_{i,c} = 138 \pm 8$ cm, but the measured adjustment length was $L_i = 90 \pm 10$ cm (figure 3a). For the sparse patch (figure 3b), $L_i = 198 \pm 10$ cm was measured for the initially flat bed, which agreed with (3.1), $L_{i,c} = 220 \pm 20$ cm. However, after the bedform developed, L_i was reduced to 146 ± 10 cm. The shortened adjustment length was attributed to the deformation of the bed near the patch leading edge (figure 3d). This finding aligned with the numerical model of a near-bank vegetation patch described in Yi *et al.* (2021), who also attributed a shortened interior adjustment length to bed deformation near the leading edge of the patch.

While the velocity within the patch declined monotonically from the leading edge, the turbulence was locally elevated, compared with the bare bed upstream of the array. Specifically, for the dense patch, turbulence was enhanced between $x = 0$ and 60 cm, relative to the bare bed region upstream of the patch, and then decayed to $k_t = 2.3 \pm 0.4 \times 10^{-4} \text{ m}^2 \text{ s}^{-2}$ for $x > L_i$ (blue symbols, [figure 3a](#)). The turbulence enhancement came from turbulence generated by stems within the array. Stem-scale turbulence is generated if stem Reynolds number $Re_d = \bar{u}d/\nu \gtrsim 100$ (Liu & Nepf 2016); here, $Re_d > 400$ over the entire array, so stem-scale turbulence was present within the array.

A region of scour began just upstream of the patch and extended into the patch over the sediment adjustment length scale, $L_s = 20 \text{ cm} < L_i$ ([figure 3c](#)), indicating that the mean velocity and turbulence intensity dropped below the threshold for sediment motion before the velocity was fully developed. This highlights how the morphological response depended on the substrate characteristics, which set the critical velocity and turbulence at which sediment motion can be initiated. Specifically, sediment mobility is dependent on grain size. For $d_{50} = 0.35 \text{ mm}$, used in the present work, the critical velocity was $U_c = 0.22 \text{ m s}^{-1}$, and the critical turbulence was $k_{t,c} = 1.2 \times 10^{-3} \text{ m}^2 \text{ s}^{-2}$, as described in § 2. The measured velocity and turbulent kinetic energy in the fully adjusted region ($x > L_i$) were lower than these critical values ([figure 3a](#)), and consistent with this, no sediment erosion was detected in this region ([figure 3c](#)).

[Figure 4](#) illustrates the spatial pattern of erosion (blue) and deposition (red) within and around both the high- and low-flow-blockage patches. Erosion (blue) was most significant within a horseshoe-shaped region at and adjacent to the leading edge of the patch. A similar pattern of erosion was observed around the leading edge of a circular patch (Follett & Nepf 2018) and at the leading edge of a rectangular patch adjacent to a channel wall (Kim *et al.* 2015a). A fraction of the sediment eroded at the leading edge was carried into the patch, creating a deposition dune within the patch (red colour at $x = 20\text{--}56$ and $39\text{--}95 \text{ cm}$ for the high- and low-flow-blockage patches, respectively; [figure 4](#)). In both patches, the volume of sediment eroded at the leading edge ($V_e = \int_0^{L_s} \int_0^b \delta_b \text{ dy dx}$) was larger than the volume deposited within the patch near the leading edge ($V_d = \int_{L_s+L_d}^{L_s+L_d} \int_0^b \delta_b \text{ dy dx}$; see [table 1](#)), indicating that only a fraction of sediment eroded at the leading edge was carried into and deposited within the patch ($V_d/V_e = 24\%$ and 55% for the high- and low-flow-blockage patches, respectively). A similar deposition mound inside the leading edge has been observed in finite patches along a sidewall (Kim *et al.* 2015a) and in submerged patches which cover the full width of the flume (Chen *et al.* 2012; Le Bouteiller & Venditti 2014; Tinoco & Coco 2016). In the previous cases, the volume of scour and deposition inside the patch increased with decreasing array density, which was attributed to the higher velocity and turbulence inside the patch at the leading edge. Consistent with these previous observations, in our study the velocity inside the low-flow-blockage patch was higher ([figure 3](#)) and resulted in larger scour and deposition (V_e , V_d in [table 1](#), [figure 3c,d](#)). Finally, along the centreline of the patch, scour and deposition were absent downstream of the deposition mound (zero net deposition; [figures 3c](#) and [3d](#)), indicating that there was no supply of sediment to this region or erosion within this region. This was consistent with the fact that both the velocity and turbulence within this region were below the mobilisation thresholds ([figures 3a](#) and [3b](#)).

Near the leading edge, erosion and deposition within the patch varied mostly in the streamwise direction and were approximately uniform across the patch width ([figure 4](#)). However, downstream of the adjustment region ($x > L_i$), the erosion and deposition pattern varied laterally across the patch width. Specifically, for the high-density patch, a flow-parallel depositional ridge was generated in the region $x > L_i = 90 \text{ cm}$ and just

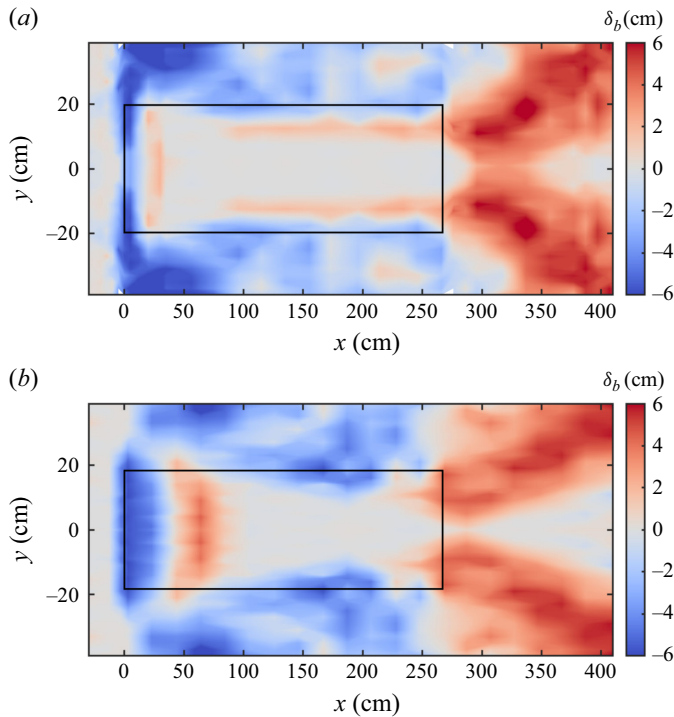


Figure 4. Net deposition (δ_b) for the (a) high-flow-blockage patch ($C_{Dab} = 3.88$) and (b) low-flow-blockage patch ($C_{Dab} = 0.91$). Grey indicates zero net deposition; red indicates positive net deposition; blue indicates negative net deposition (net erosion). The solid rectangle indicates the limits of the array.

inside the flow-parallel edge (red region along the patch edge; [figure 4a](#)). In contrast, a depositional ridge did not form along the flow-parallel edge for the low-density patch ([figure 4b](#)). This difference was not associated with lateral transport at the patch edge. Specifically, in the region of fully adjusted flow, the time-mean lateral velocity (\bar{v}) at the patch edge was negligible for both patches ([figure 5a](#)), as expected for $d\bar{u}/dx = 0$ ([figure 3a,b](#)), and thus the time-averaged velocity field cannot explain the difference in bed morphology between the two patches. The oscillating component of lateral velocity (v_{rms}) along the patch edge was also similar between the two patches ([figure 5b](#)). Thus, the difference in flow-parallel ridge formation was most likely due to the difference in time-averaged streamwise velocity and turbulence within the patch, both of which were higher inside the low-flow-blockage patch ($y/b < 1$ in [figures 5c](#) and [5d](#)). The formation of the flow-parallel ridge is discussed in more detail in the next section.

Finally, for the low-flow-blockage patch, deposition within the patch was observed very close to the end of the patch ([figure 4b](#); red regions between $x = 210$ and 265 cm), which was likely due to flow recirculation in the lee of the patch. Although negative velocity was not observed at the centreline, the velocity did go to zero downstream of the patch ([figure 3b](#)). To evaluate whether the ridges were associated with the trailing edge of the patch, we extended the patch to $L = 385$ cm, and the position of the deposition region moved downstream, again associated with the trailing edge ([figure S7](#) of the supplementary material), which confirmed that the ridges were associated with the trailing edge. Finally, sediment eroded within and adjacent to the patch was transported downstream, producing a V-shaped depositional mound after the patch ([figure 4a](#)). Because no sediment collected in the sediment trap, we concluded that no sediment was

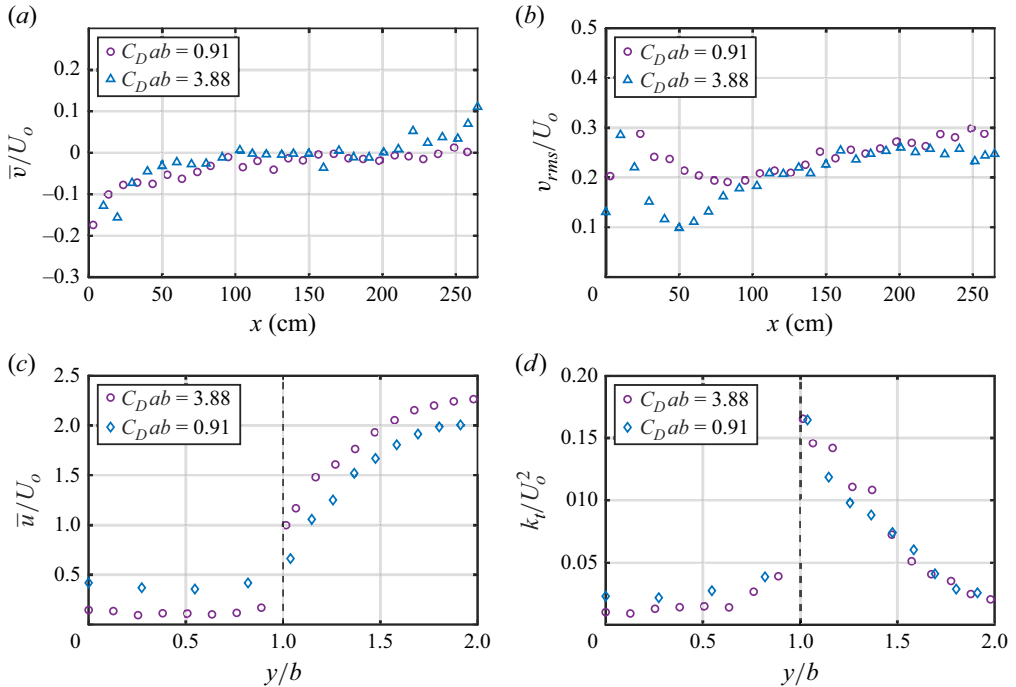


Figure 5. Longitudinal profiles along the flow-parallel edge at $y = b$: (a) time-averaged spanwise velocity (\bar{v}) and (b) fluctuating spanwise velocity (v_{rms}). Lateral profiles of (c) time-averaged streamwise velocity (\bar{u}) and (d) turbulent kinetic energy (k_t) in the fully developed region ($x > L_i$).

transported beyond $x = 480$ cm. That is, while the patch generated a significant local redistribution of sediment, extending over $1.8L$, it did not produce channel-scale transport. A similar local redistribution of sediment was also observed in Follett & Nepf (2012).

3.2. The formation of a flow-parallel depositional ridge

For the high-flow-blockage patch, a flow-parallel depositional ridge formed just inside the flow-parallel edge in the fully developed region ($x > L_i$; figure 4a). The formation and position of the ridge were associated with the shear layer along the patch edge. Flow diversion away from the high drag within the patch created a velocity difference (figure 6a) between the free stream adjacent to the patch ($y > b$) and the patch interior ($y < b$), which contributed to the formation of coherent structures by KH instability. The vortices penetrated the vegetated region over distance δ_I , and grew into the free stream over distance δ_O . The PSD of the transverse velocity (v) indicated a dominant frequency close to that predicted for KH instability, $f_{KH}\theta/\bar{U} = 0.032$ (Ho & Huerre 1984) (figure 6b). However, based on the lateral profile of streamwise velocity and shear stress (figure 6a), the KH structures and associated turbulent transport did not penetrate into the patch beyond the first row of dowels. Specifically, δ_I was smaller than 2.5 cm, which was the distance from the patch edge to the first measurement point within the array. Note that the depositional ridge formed farther into the patch, between 7.5 and 12.5 cm from the patch edge, such that transport associated with shear-layer turbulence cannot explain the extent of cross-stream sediment transport needed to form the ridge.

A second mechanism of cross-stream transport likely contributed to the formation of the depositional ridge, associated with the wave motion induced by the passage of the vortices along the patch edge (White & Nepf 2007; Zong & Nepf 2011). Specifically, the centre of

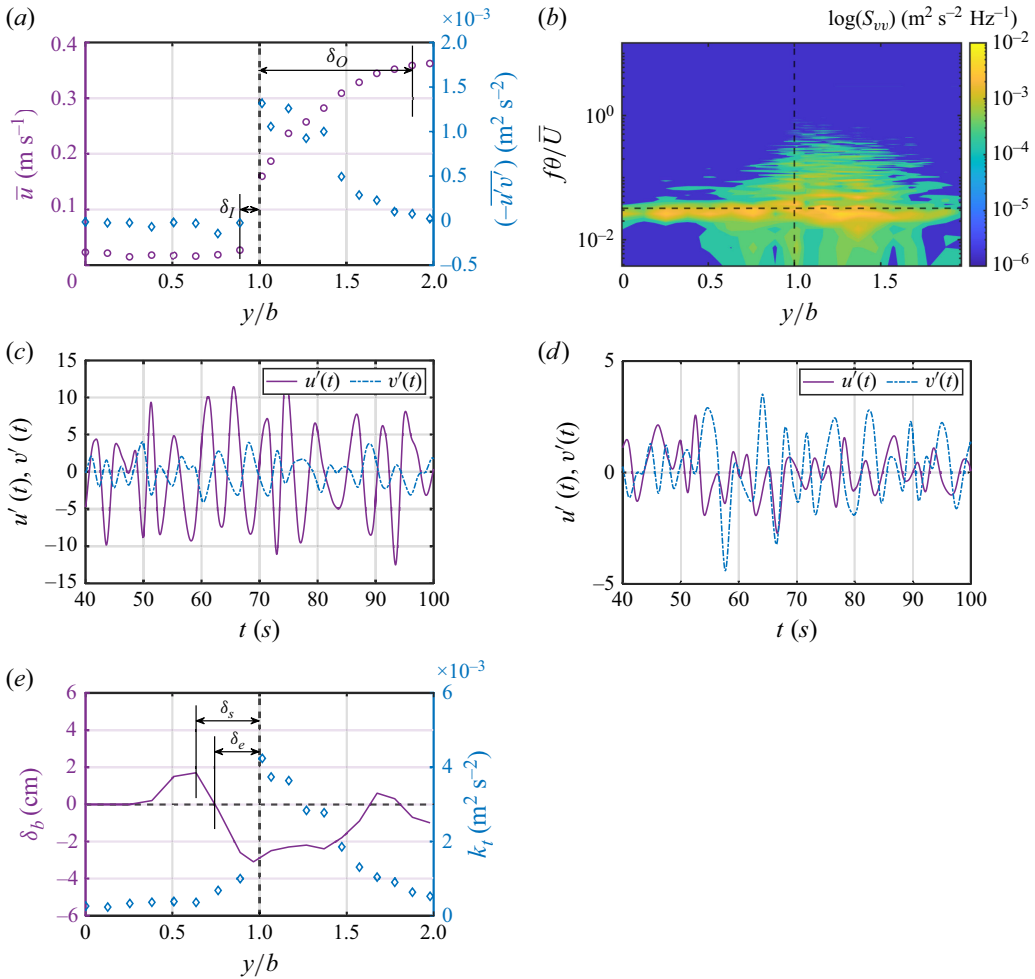


Figure 6. Conditions contributing to the formation of an edge-parallel ridge within the fully developed region ($x > L_i$) of the high-flow-blockage patch ($C_{Dab} = 3.88$). (a) Lateral profiles of time-averaged streamwise velocity (\bar{u}) and Reynolds shear stress ($-\overline{u'v'}$). (b) Magnitude of PSD of cross-stream velocity (v), shown by colour bar, distributed by lateral position and frequency. The horizontal dashed line indicates expected KH frequency, $f_{KH}\theta/\bar{U} = 0.032$. The time series of fluctuating streamwise ($u'(t)$) and transverse ($v'(t)$) velocity (c) at 1 cm outside the patch and (d) within the patch ($y = b - \delta_s$). (e) Lateral profiles of net deposition (δ_b) and turbulent kinetic energy (k_t). The horizontal black dashed line indicates the initial bed elevation, $\delta_b = 0$. The vertical dashed line indicates the lateral interface of the array ($y = b$).

each KH vortex is a point of low pressure, whose passage along the patch edge generates an oscillating response within the array (White & Nepf 2007). Necessarily, the frequency of the vortex-induced wave response is the same as that of the vortex passage, so that peaks in the PSD of the cross-stream velocity were consistent across the patch width (figure 6b). The wave response was apparent in the velocity records. Specifically, within the patch interior, there was a phase shift of $\pi/2$ rad between the fluctuating streamwise velocity (u') and fluctuating transverse velocity (v'), as shown in figure 6(d), which is consistent with a wave motion. In contrast, within the shear layer (e.g. 1 cm outside the patch) u and v were anticorrelated, consistent with the higher Reynolds stress of the shear layer (figure 6c).

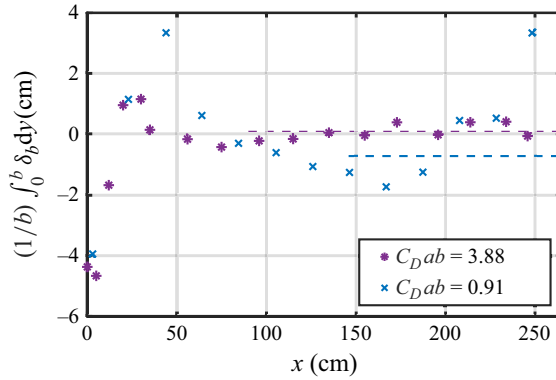


Figure 7. The laterally averaged net deposition $(1/b) \int_0^b \delta_b dy$ at each streamwise position along the array. The dashed horizontal line represents the average value in the fully developed region ($x > L_i$).

Lateral transport associated with the wave response likely contributed to the formation and location of the depositional ridge inside the dense patch ($y = b - \delta_s$). Similarly, Zong & Nepf (2011) showed that the vortex-induced wave response along a patch edge contributed to the delivery and deposition of suspended material within the patch, allowing sediment to be delivered to regions inside the patch not directly accessible by turbulent flux. Note that the lateral position of the ridge was constant over the length of the patch (figure 4a), which was consistent with the uniform wave response (v_{rms} ; figure 5b) along the patch edge. A weaker wave motion in the central region of the vegetation patch (figure 6b) restricted the delivery of sediment to the patch centreline. Consequently, despite the reduction in turbulence and velocity in this area ($x > L_s + L_d$, $-7.5 \text{ cm} < y < 7.5 \text{ cm}$; figure 6a,e), no sediment deposition occurred.

Elevated turbulence and velocity near the streamwise edge of the patch produced erosion (blue, figure 4). For the dense patch, the erosion extended over the distance $\delta_e = 5.0 \pm 1.3 \text{ cm}$ into the patch, which was consistent with the region of elevated turbulent kinetic energy (figure 6e). However, in the fully developed region, the net deposition averaged across the dense patch width was zero within uncertainty ($(1/b) \int_0^b \delta_b dy = 0.8 \pm 0.8 \text{ mm}$), indicating that the depositional ridge inside the patch was created from sediment eroded at the interfaces, and did not represent new sediment arriving from outside the patch (figure 7). In contrast, for the sparse patch, $(1/b) \int_0^b \delta_b dy = -7.2 \pm 0.3 \text{ mm}$, indicating a net loss of sediment from the patch. In this case, material eroded near the edge was carried out of the patch.

Finally, outside the patch ($y > b$), elevated turbulence and velocity produced significant scour (figure 6e). Although the velocity was higher outside the shear layer ($y > b + \delta_O$) (figure 6a), the scouring was more significant directly adjacent to the array ($y < b + \delta_O$). In fact, the velocity in the patch-adjacent region was lower than the critical velocity for sediment motion on bare bed, $\bar{u} < U_c = 0.22 \text{ m s}^{-1}$. However, the turbulence adjacent to the patch was above the critical magnitude, $k_t > k_{t,c} = 1.2 \times 10^{-3} \text{ m}^2 \text{ s}^{-2}$, over the region $y = 17$ to 32 cm , consistent with region of scour ($\delta_b < 0$; figure 6e), indicating that the elevated turbulence was triggering the erosion at the patch edge.

3.3. The influence of stem diameter on interfacial shear layer

For both patch densities ($C_{Da} = 4.9$ and 19.7 m^{-1}), the shear layer at the patch lateral edge had a limited extension into the array. Specifically, the inner penetration length $\delta_I < 2.5 \text{ cm}$

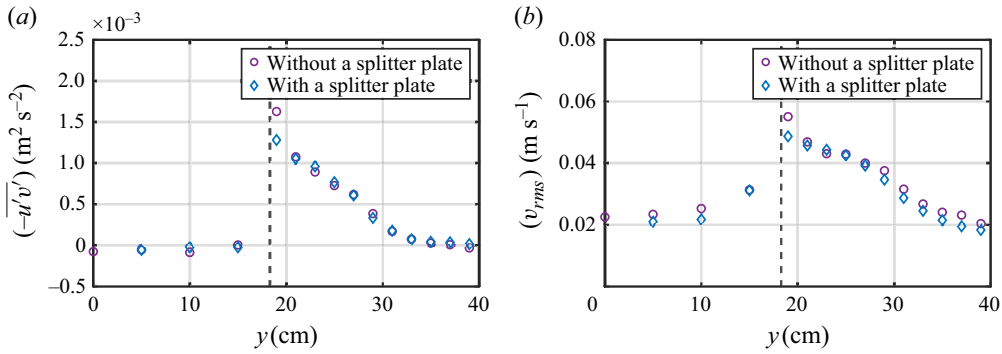


Figure 8. The lateral profiles of (a) Reynolds shear stress ($-\overline{u'v'}$) and (b) fluctuating spanwise velocity (v_{rms}) for low-density patch with and without a splitter plate at the patch centreline. The dashed lines indicate the lateral interface of the patch, $y = b$.

(figures 6a and 8a). The dowel diameter was $d = 1.27$ cm, similar to δ_I , suggesting that the KH vortices and associated shear layer did not penetrate past the first row of the dowels. This stands in sharp contrast to previous studies of rectangular patches constructed with a smaller dowel diameter, $d = 0.64$ cm, but the same range of $C_D a$, which exhibited a strong dependence between δ_I and $C_D a$. Specifically, Rominger & Nepf (2011) observed that δ_I decreased from 10 to 2 cm when $C_D a$ increased from 5.3 to 20 m^{-1} , which was consistent with the theoretical and empirical formula given in White & Nepf (2008), $\delta_I = \max[0.5(C_D a)^{-1}, 1.8d] = 9.5$ and 2.5 cm, respectively. The limited penetration of the shear layer in the present study was likely due to the locally stronger shear created by the larger and in-line dowels, compared with the smaller and staggered arrangement used in previous studies. Specifically, the locally intense shear generated by the in-line wakes of dowels along the edge of the patch produced shear sheltering, which blocked the penetration of the KH vortices into the patch (Hunt & Durbin 1999; Ptasinski *et al.* 2003).

Further, for patches constructed with smaller dowels (e.g. Rominger & Nepf 2011), the KH vortices along the two flow-parallel interfaces interacted across the patch width when $C_D ab < 2$, and this enhanced the Reynolds stress. However, this interaction was not observed for the low-flow-blockage patch ($C_D ab = 0.91$) in the present study. Specifically, we compared the lateral distribution of Reynolds stress and v_{rms} between scenarios in which the vortices were able to communicate across the patch, and scenarios in which this communication was blocked by a splitter plate placed at the patch centreline. The lateral profiles of $-\overline{u'v'}$ and v_{rms} with and without a splitter plate were nearly identical (figure 8), with a 10 % and 20 % change only at the peak values for v_{rms} and $-\overline{u'v'}$, respectively. This was a much smaller change than the 35 % and 85 % reductions, respectively, observed with the addition of a centreline plate in Rominger & Nepf (2011). This comparison suggested that vortex synchronisation across the patch width did not occur in the present study. This was likely due to the restriction of KH penetration into the patch by shear sheltering. This is a key new result that indicates how patch velocity structure can be influenced by the size and arrangement of the elements within the patch.

3.4. Deposition in the patch wakes

Directly downstream of the high-flow-blockage patch, the side-parallel depositional ridges ($y = b \pm \delta_s$) grew towards the centreline, enclosing a region of no bed elevation change (grey colour in figure 4) between $x = 270$ and 290 cm. Even though flow conditions

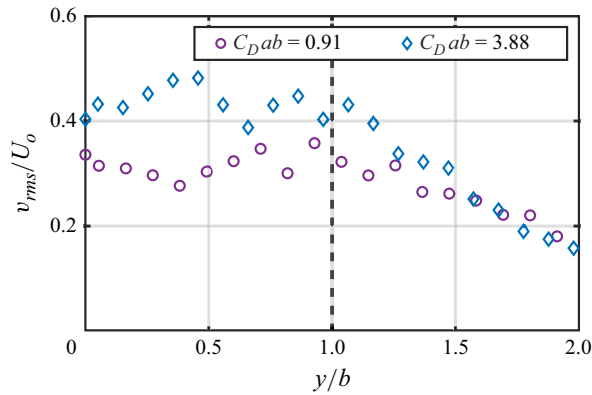


Figure 9. Lateral profiles of normalised fluctuating cross-stream velocity (v_{rms}/U_o) at $x = 318$ and 328 cm, i.e. 50 and 60 cm after the trailing edge of the high-flow-blockage patch and low-flow-blockage patch, respectively. The dashed line indicates the half-width of the patch, $y = b$.

within this zone were favourable for deposition, with $\bar{u} < U_c$ and $k_t < k_{t,c}$, no sediment was supplied by bedload to this region, and thus net deposition was zero. However, this region did accumulate the fine suspended material present in the flume (residual rust particles), which was evident by the change in surface colour from sand to reddish brown (figure 11*b–d*). Specifically, note the reddish brown triangular region at the end of the patch, visible in the lower part of figure 11(*d*). A similar region of zero net deposition was observed directly downstream of a rectangular patch located along a sidewall (Kim *et al.* 2015*a*) and a high-flow-blockage circular patch (Follett & Nepf 2012). Further, Follett & Nepf (2012) also observed the accumulation of suspended sediment in this region.

Farther downstream from a patch, the sediment scoured from around the patch is deposited (e.g. Follett & Nepf 2012; Kim *et al.* 2015*a*). The spatial distribution of net deposition in the wake is dependent on local sediment transport capacity, dictated by velocity and turbulence, and also on the sediment characteristics (Okhravi *et al.* 2023). For example, downstream of the high-flow-blockage circular patch described in Follett & Nepf (2012) deposition occurred on the centreline, whereas in the wake of the rectangular patch in this study, deposition was mostly distributed away from the centreline. In the case of Follett & Nepf (2012), a strong von Kármán vortex street was present in the patch wake and carried material eroded around the patch towards the centreline, which is similar to the mechanism producing a depositional mound on the centreline behind a solid circular obstruction (Dargahi 1990; Yagci *et al.* 2017). In this study, net deposition did not peak at the centreline, but peaked at a point 8.7 cm inward from the patch edge (darkest red downstream of patch in figure 4*a*), which was less than the wake half-width. This suggested that the lateral transport in the wake was less than the half-width of the patch. For the dense patch, the fluctuating transverse velocity in the wake was $v_{rms} = 6.9 \text{ cm s}^{-1}$ (figure 9), with frequency $f_{VK} = 0.16 \text{ Hz}$. The lateral transport associated with this motion can be estimated by the wave orbital radius of the oscillating lateral velocity (Luhar & Nepf 2016), $A_w = \sqrt{2}v_{rms}/2\pi f_{VK} = 9.7 \text{ cm}$, which was less than the patch half-width, $b = 19.7 \text{ cm}$. The stronger lateral oscillation, indicated by higher v_{rms} (figure 9), in the wake of the high-flow-blockage patch resulted in sediment transported further inward towards the centreline, when compared to the low-flow-blockage patch (figure 4). Specifically, the distance from the side edge of the patch to the position where the depositional mound peaked was 8.7 and 7.3 cm for the dense and sparse patch, respectively.

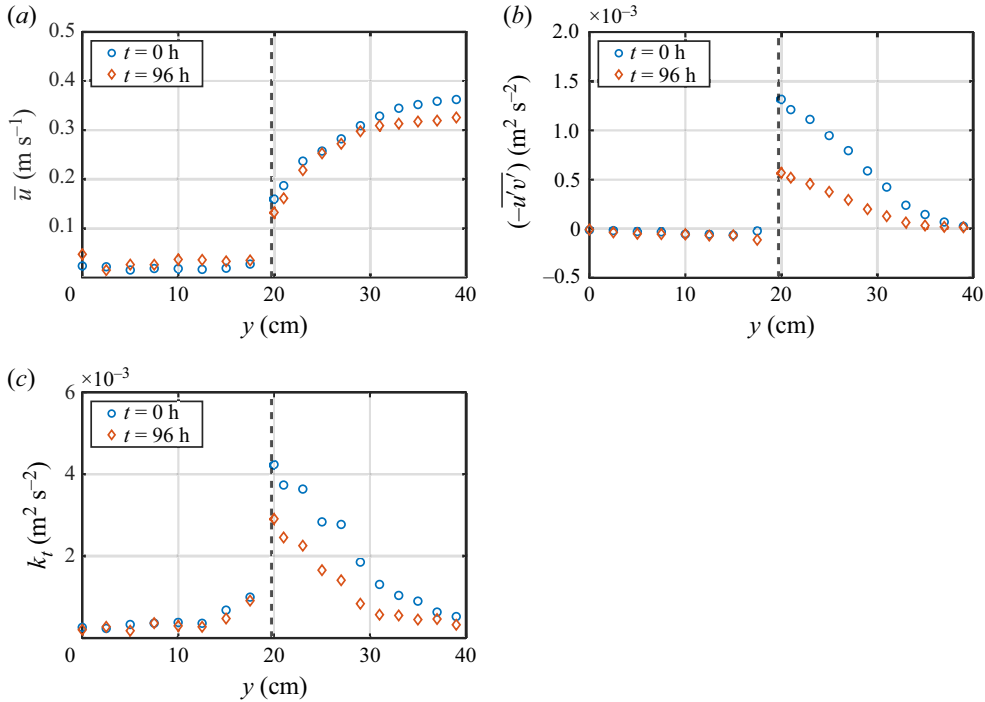


Figure 10. Comparison of flow statistics with initially flat bed ($t = 0$, blue circles) and with fully developed bedforms ($t = 96$ h, orange symbols). (a) Time-averaged streamwise velocity (\bar{u}), (b) Reynolds shear stress ($-\overline{u'v'}$) and (c) turbulent kinetic energy (k_t). Profiles measured at $x = 249$ cm in the fully developed region of the patch ($x > L_i$) for high-flow-blockage canopy ($C_{Dab} = 3.88$). The vertical dashed line indicates the lateral interface of the array, $y = b$.

Farther downstream from the patch, the V-shaped mound widened (figure 4). This expanding, V-shaped deposition pattern was also observed in a low-flow-blockage circular patch (Follett & Nepf 2012; Yagci *et al.* 2017) and a square array (Kim *et al.* 2015b), and was attributed to the absence of, or weakness of, the wake vortices (Follett & Nepf 2012). Specifically, the lateral velocity needed to carry the sediment to the centreline was absent or too weak. Note that we do not believe the deposition pattern in the present study was linked to the ratio of array width to channel width (40 % in the present study), because the same pattern of separated deposition mounds was also present when the ratio of patch diameter to channel width was less than 18 % (Follett & Nepf 2012).

3.5. Feedback from morphological evolution to wake velocity structure

To illustrate how the evolution of the bed morphology altered the flow structure, conditions with the initial flat bed ($t = 0$) and with fully developed bedforms ($t = 96$ h) are compared in figure 10. First, erosion adjacent to the patch (figure 4) increased the local flow depth by 3 cm and generated bedforms with an amplitude of 2 cm. The increase in flow depth tended to decrease the flow resistance, but the introduction of bedforms tended to increase it. These competing affects appeared to balance in the present study, as the distribution of velocity between the patch and adjacent open channel did not change significantly between the flat bed and deformed bed (compare blue and orange symbols, respectively, in figure 10a). However, the change in flow depth and introduction of bedforms diminished the coherence of the shear-layer vortices along the flow-parallel edge, which was indicated

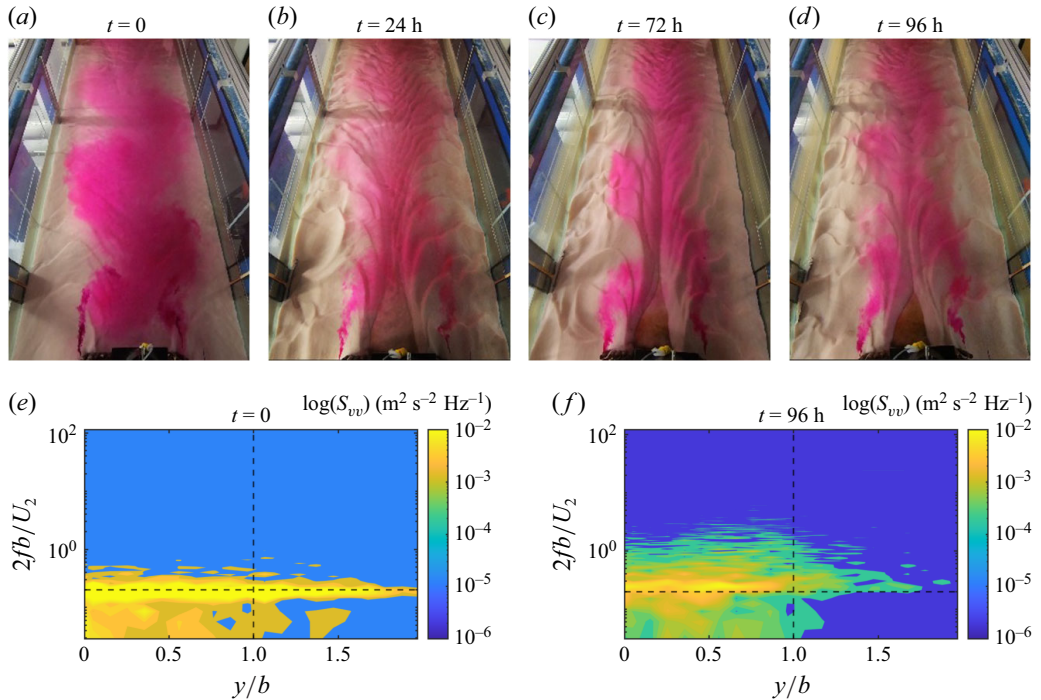


Figure 11. (a–d) As bedforms in the wake grew, the vortex street in the wake was weakened, as illustrated by dye visualisation. (e, f) The PSD in the wake over flat bed ($t = 0$) and over deformed bed ($t = 96$ h), measured at $x = 318$ cm, which was 50 cm downstream of the trailing edge of the patch and close to the peak of the deposition (figure 4a). The horizontal dashed line indicates the dimensionless frequency of a von Kármán vortex, $2f_{VK}b/U_2 = 0.2$. The vertical dashed line indicates the lateral interface of the array.

in a diminished Reynolds stress (figure 10b) and turbulence (figure 10c). Because the shear across the flow-parallel patch edges was not significantly reduced (figure 10a), the diminished coherence in the shear-layer vortices was likely due to the introduction of bedforms, associated with a 15 % variation in water depth in the open-channel region.

Similarly, the change in bed morphology in the wake led to a change in the von Kármán vortex street, which was revealed through dye visualisation. With the initially flat bed, a strong von Kármán vortex street was observed in the wake, spanning the entire channel width (figure 11a). However, as the bedforms evolved in the wake, the von Kármán vortex street became more narrow and less coherent over time (figure 11b–d). In particular, note the change directly downstream of the patch. At $t = 0$, the von Kármán vortex street formed close to the patch and carried tracer upstream to the trailing edge of the patch. At this time, a recirculation zone ($\bar{u} < 0$) was present at the centreline, directly behind the patch (figure 12a; $t = 0$). However, at later times ($t > 24$ h), the vortex street formed at a distance from the patch, and no tracer was carried into the region directly behind the patch (figure 11d). In addition, no recirculation was detected in the wake (figure 12a). Further, fine-particle deposition occurred in this region, which was visualised by the dark brown colour of the depositing material. Specifically, between $t = 24$ and 96 h, a triangular region directly behind the patch became increasingly darker in colour (see figure 11c,b,d). The progressive decline in von Kármán vortex strength and coherence was manifest in reduced v_{rms} (figure 12b), reduced turbulent kinetic energy (figure 12c) and a reduced PSD peak magnitude (compare figure 11e,f). Note that, even as the strength of the vortex street

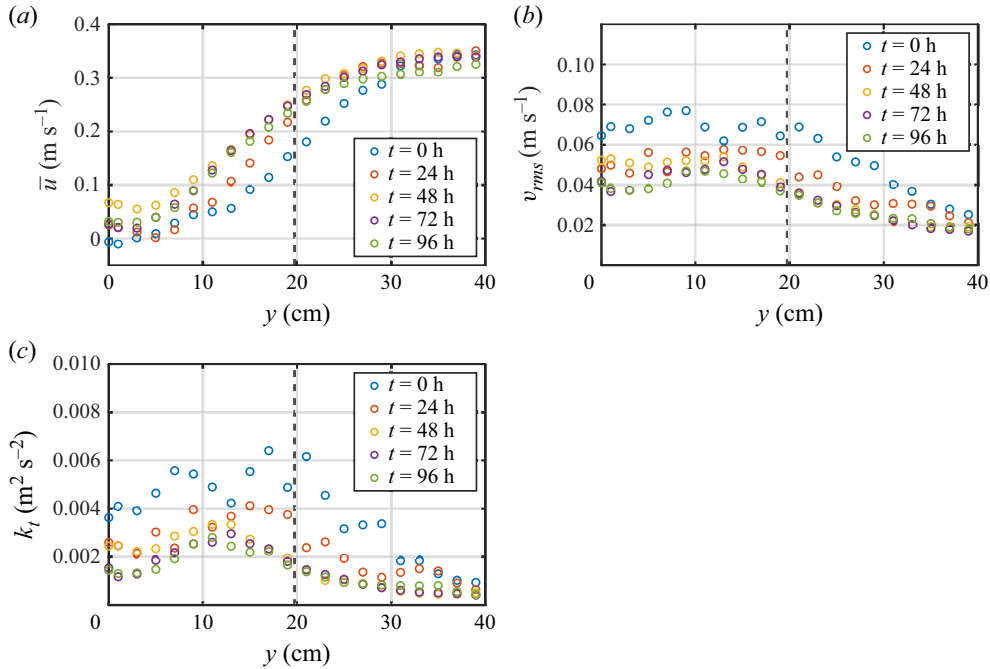


Figure 12. The lateral distribution of (a) time-averaged streamwise velocity (\bar{u}), (b) fluctuating spanwise velocity (v_{rms}) and (c) turbulent kinetic energy (k_t) at $x = 318$ cm, i.e. 50 cm after the trailing edge of the patch. The dashed lines indicate the half-width of the patch, $y = b$.

declined, the dominant frequency remained the same, $St_b = 2f_{VK}b/U_2 = 0.2$, which was consistent with similar observations behind circular porous arrays (Zong & Nepf 2012).

4. Discussion

4.1. The decay of wake vortex with bedform evolution

The creation of bedforms in the wake increased the bed friction coefficient (C_f) and diminished the local flow depth, both of which influenced the wake vortex stability. Consider the wake stability parameter $S = C_f W/h$, defined by Chen & Jirka (1995), which indicates when bed friction suppresses the generation of a von Kármán vortex street. For the high-flow-blockage patch, the wake bedforms grew to a height of $\Delta = 6$ cm and length of $\Lambda = 41$ cm, reducing the water depth from $h = 20$ to 14 cm. Based on (2.1), this enhanced the bed friction coefficient from 0.005 to 0.023. As a result, the wake instability parameter, S , changed from 0.01 to 0.07, approaching the critical value $S_c = 0.09$ at which wake vortices were suppressed behind porous plates ($\Phi = 0.5$; Chen & Jirka 1995). Previous studies have also observed that the wake vortex behind a circular patch (Chang *et al.* 2017) and a solid cylinder (Kirkil *et al.* 2008) was weakened as wake bedforms developed. These studies attributed the vortex decay to upwelling mean flow generated by a bedform on the wake centreline. The upwelling flow impeded the interactions of the stream-parallel shear layers, which is the precursor to wake vortex formation, resulting in the two separated shear layers persisting in the wake (Kirkil *et al.* 2009). In the present experiment, the bedforms were not located on the centreline, and, although the vertical velocity was measured at various locations, no upwelling flow was detected. Thus, the decay of the wake vortex in the present work was likely not influenced by the upwelling flow.

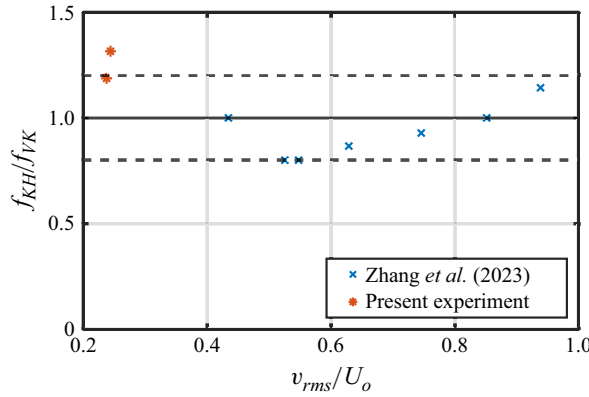


Figure 13. Ratio of the von Kármán vortex street frequency, f_{VK} , in the patch wake to the frequency of the KH vortices along the patch edge, f_{KH} . The solid line indicates $f_{VK} = f_{KH}$ and the dashed lines indicate $\pm 20\%$ deviation.

4.2. Vortex frequency alignment

In the present experiment, and in the recent similar experiments reported in Zhang *et al.* (2023), the frequency of the KH vortices (f_{KH}) at the patch side edges and the frequency of the von Kármán vortices (f_{VK}) in the patch wakes were the same to within $\pm 20\%$ (figure 13). In the previous study, which used a smaller cylinder diameter ($d = 3.2$ mm), the synchronisation was attributed to the interaction between the KH vortices formed on the two flow-parallel edges and the von Kármán vortex in the wake (Zhang *et al.* 2023). Specifically, the measured f_{KH} and f_{VK} were higher and lower than the predicted value (table 2), respectively, but they matched each other, $f_{KH} = f_{VK}$. In the present study, there was no interaction between the parallel shear layers and KH vortices across the patch width (figure 8), which was attributed, in part, to the larger stem size, which produced an edge shear layer strong enough to produce shear sheltering that inhibited the penetration of the KH vortices into the patch. Further, the measured f_{KH} and f_{VK} each matched their theoretical values (table 2). Specifically, Ho & Huerre (1984) showed that KH vortices within a shear layer have a frequency defined by the momentum thickness (θ) and the minimum and maximum velocity in the shear layer (U_1 and U_2 , respectively):

$$f_{KH} = \frac{0.032(U_1 + U_2)}{2\theta}, \quad (4.1)$$

which has been demonstrated to predict KH vortex frequency in vegetated channels with emergent cylinders (White & Nepf 2008) and for submerged canopies of rigid and flexible plant models (Ghisalberti & Nepf 2002). In addition, based on a large literature for cylinder wakes, the Strouhal number $St = fD/U \approx 0.2$ for $200 < Re < 3 \times 10^5$ (Roshko 1961; Schewe 1983). Zong & Nepf (2012) confirmed this for a von Kármán vortex street behind a circular patch of cylinders, i.e.

$$f_{VK} = \frac{0.2U_2}{2b}. \quad (4.2)$$

Table 2 shows that the observed frequencies for both f_{KH} and f_{VK} agreed with the predictions ((4.1) and (4.2)) within uncertainty, suggesting that the similarity between f_{KH} and f_{VK} was a coincidence, and not driven by mutual interaction. The absence of vortex synchronisation was consistent with the absence of KH connection across the patch in the present work (see figure 8).

	f_{KH} (Hz)		f_{VK} (Hz)	
	Predicted f_{KH} (4.1)	Peak in PSD in the patch	Predicted f_{VK} (4.2)	Peak in PSD in the wake
Dense	0.21 (0.02)	0.19 (0.03)	0.17 (0.01)	0.16 (0.03)
Sparse	0.25 (0.06)	0.25 (0.03)	0.17 (0.01)	0.19 (0.03)
ZA5*	0.04 (0.01)	0.12 (0.01)	0.22 (0.01)	0.15 (0.01)
ZB5*	0.04 (0.01)	0.16 (0.01)	0.23 (0.01)	0.14 (0.01)
ZC4*	0.04 (0.01)	0.13 (0.01)	0.23 (0.01)	0.15 (0.01)
ZC5*	0.03 (0.01)	0.14 (0.01)	0.23 (0.01)	0.14 (0.01)
ZD3*	0.05 (0.01)	0.14 (0.01)	0.23 (0.01)	0.14 (0.01)
ZD4*	0.04 (0.01)	0.13 (0.01)	0.23 (0.01)	0.14 (0.01)
ZD5*	0.03 (0.01)	0.12 (0.01)	0.17 (0.01)	0.15 (0.01)

Table 2. The predicted and measured frequencies for KH vortices (f_{KH}) and von Kármán vortices (f_{VK}). The asterisk (*) indicates the data measured by Zhang *et al.* (2023). Numbers in parentheses are uncertainties.

Finally, we also considered the possible role of stem-scale vortices. For the dense patch, in the fully developed region, the frequency of the stem-scale von Kármán vortices was observed in PSD, $f_d = 0.85$ (figure S8 of the supplementary material), which was consistent with $f_d = (StU_1)/d = 0.8$, with $St = 0.2$ and $U_1 = 0.05 \text{ m s}^{-1}$. Then, $f_d/f_{VK} = (StU_1/d)/(StU_2/2b) = (2bU_1/U_2d)$. In this case, $U_2 = 0.35 \text{ m s}^{-1}$, so $f_d/f_{VK} = 4.4$, indicating that $f_d \gg f_{VK} \approx f_{KH}$. The difference between the stem-scale frequency and KH frequency is also illustrated in figure S8 of the supplementary material. This difference suggested that the stem-scale vortex shedding did not influence the patch-scale von Kármán vortex street.

5. Summary

This study experimentally investigated the velocity field and bedform development within and around a rectangular patch of model emergent vegetation. The patch was simulated by rigid dowels arranged in a regular pattern, with two densities representing high- and low-flow-blockage conditions. An 8 cm layer of sand covered the test section. Velocity measurements and dye visualisation were conducted at different running time to evaluate the flow response.

Near the leading edge of the patch, stem-generated turbulence enhanced local turbulent kinetic energy, even as the time-mean velocity decreased. The elevated turbulent kinetic energy produced sediment erosion. A fraction of the eroded sediment was carried downstream into the patch, creating an interior deposition dune. The dune was smaller inside the denser patch, compared with the more sparse patch, because less sediment was eroded and a larger fraction of eroded sediment was transported out of the patch by the strong lateral flow diversion.

In the fully developed region, KH vortices were initiated within the shear layers developed along the side edges of the patch. However, for both the sparse and dense patches, these vortices were blocked by shear sheltering at the patch edge, and did not penetrate beyond the first row of dowels. Elevated turbulence at the patch edge caused sediment erosion. For the dense patch, the eroded sediment was transported into the patch by the vortex-induced wave response, creating flow-parallel deposition ridges. The process of ridge formation was only a redistribution of sediment, producing no net change in

sediment volume within the patch. In contrast, for the sparse patch, sediment scoured at the patch edge was carried away, leading to sediment loss from the patch.

Sediment eroded from the regions around the patch was deposited in the wake. Because the von Kármán vortex street was weak, the lateral transport in the wake was limited to less than the patch half-width. As a result, the deposition occurred closer to the wake edge, and not on the wake centreline. The formation of bedforms and the associated increase in bed friction progressively diminished the von Kármán vortex street, due to the enhanced bed friction associated with the deformed bed and reduced water depth. Finally, although the patch generated a significant local redistribution of sediment, it did not provoke channel-scale sediment transport. From the perspective of natural sustainability, a denser patch is recommended to improve sediment retention within the patch.

Supplementary material. Supplementary material is available at <https://doi.org/10.1017/jfm.2025.10492>.

Funding. This research was supported by the Hong Kong Research Grants Council (RGC) under Project No. C5002-22Y.

Declaration of interests. The authors report no conflict of interest.

Data availability statement. Data presented in this paper are available on <https://doi.org/10.6084/m9.figshare.29995297.v1>.

REFERENCES

- ABERLE, J. & JÄRVELÄ, J. 2013 Flow resistance of emergent rigid and flexible floodplain vegetation. *J. Hydraul. Res.* **51** (1), 33–45.
- BOUMA, T.J., *et al.* 2016 Short-term mudflat dynamics drive long-term cyclic salt marsh dynamics. *Limnol. Oceanogr.* **61** (6), 2261–2275.
- BOUMA, T.J., VAN DUREN, L.A., TEMMERMAN, S., CLAVERIE, T., BLANCO-GARCIA, A., YSEBAERT, T. & HERMAN, P.M.J. 2007 Spatial flow and sedimentation patterns within patches of epibenthic structures: combining field, flume and modelling experiments. *Cont. Shelf Res.* **27** (8), 1020–1045.
- CHANG, W.-Y., CONSTANTINESCU, G. & TSAI, W.F. 2017 On the flow and coherent structures generated by a circular array of rigid emerged cylinders placed in an open channel with flat and deformed bed. *J. Fluid Mech.* **831**, 1–40.
- CHEN, D. & JIRKA, G.H. 1995 Experimental study of plane turbulent wakes in a shallow water layer. *Fluid Dyn. Res.* **16** (1), 11–41.
- CHEN, S.-C., CHAN, H.-C. & LI, Y.-H. 2012 Observations on flow and local scour around submerged flexible vegetation. *Adv. Water Resour.* **43**, 28–37.
- COLEMAN, J.M., HUH, O.K. & BRAUD, D.W. Jr. 2008 Wetland loss in world deltas. *J. Coast. Res.* **24** (10024), 1–14.
- COLOMBINI, M. & STOCCHINO, A. 2012 Three-dimensional river bed forms. *J. Fluid Mech.* **695**, 63–80.
- DARGAHI, B. 1990 Controlling mechanism of local scouring. *J. Hydraul. Engng* **116** (10), 1197–1214.
- ELSEY-QUIRK, T., LYNN, A., JACOBS, M.D., DIAZ, R., CRONIN, J.T., WANG, L., HUANG, H. & JUSTIC, D. 2024 Vegetation dieback in the Mississippi river delta triggered by acute drought and chronic relative sea-level rise. *Nat. Commun.* **15** (1), 3518.
- FAGHERAZZI, S., BRYAN, K.R. & NARDIN, W. 2017 Buried alive or washed away: the challenging life of mangroves in the Mekong delta. *Oceanography* **30** (3), 48–59.
- FOLLETT, E. & NEPF, H. 2018 Particle retention in a submerged meadow and its variation near the leading edge. *Estuar. Coast.* **41**, 724–733.
- FOLLETT, E.M. & NEPF, H.M. 2012 Sediment patterns near a model patch of reedy emergent vegetation. *Geomorphology* **179**, 141–151.
- GHISALBERTI, M. & NEPF, H.M. 2002 Mixing layers and coherent structures in vegetated aquatic flows. *J. Geophys. Res.: Oceans* **107** (C2), 3–1–3–11.
- GORING, D.G. & NIKORA, V.I. 2002 Despiking acoustic Doppler velocimeter data. *J. Hydraul. Engng* **128** (1), 117–126.
- GU, J., SHAN, Y., LIU, C. & LIU, X. 2019 Feedbacks of flow and bed morphology from a submerged dense vegetation patch without upstream sediment supply. *Environ. Fluid Mech.* **19**, 475–493.
- GURNELL, A. 2014 Plants as river system engineers. *Earth Surf. Process. Landf.* **39** (1), 4–25.

- HO, C.M. & HUERRE, P. 1984 Perturbed free shear layers. *Annu. Rev. Fluid Mech.* **16**, 365–424.
- HUNT, J.C.R. & DURBIN, P.A. 1999 Perturbed vortical layers and shear sheltering. *Fluid Dyn. Res.* **24** (6), 375.
- JAMES, C.S., BIRKHEAD, A.L., JORDANOVA, A.A. & O'SULLIVAN, J.J. 2004 Flow resistance of emergent vegetation. *J. Hydraul. Res.* **42** (4), 390–398.
- JULIEN, P.Y. 2010 *Erosion and Sedimentation*. Cambridge University Press.
- KIM, H.S., KIMURA, I. & SHIMIZU, Y. 2015a Bed morphological changes around a finite patch of vegetation. *Earth Surf. Process. Landf.* **40** (3), 375–388.
- KIM, H.S., NABI, M., KIMURA, I. & SHIMIZU, Y. 2015b Computational modeling of flow and morphodynamics through rigid-emergent vegetation. *Adv. Water Resour.* **84**, 64–86.
- KIRKIL, G. & CONSTANTINESCU, G. 2010 Flow and turbulence structure around an in-stream rectangular cylinder with scour hole. *Water Resour. Res.* **46** (11), W11549.
- KIRKIL, G., CONSTANTINESCU, G. & ETTEMA, R. 2009 Detached eddy simulation investigation of turbulence at a circular pier with scour hole. *J. Hydraul. Engng* **135** (11), 888–901.
- KIRKIL, G., CONSTANTINESCU, S.G. & ETTEMA, R. 2008 Coherent structures in the flow field around a circular cylinder with scour hole. *J. Hydraul. Engng* **134** (5), 572–587.
- KONDIOLKA, J.M. & NEPF, H.M. 2014 Vegetation wakes and wake interaction shaping aquatic landscape evolution. *Limnol. Oceanogr.: Fluids Environ.* **4** (1), 106–119.
- LARSEN, L.G. & HARVEY, J.W. 2010 How vegetation and sediment transport feedbacks drive landscape change in the everglades and wetlands worldwide. *Am. Nat.* **176** (3), E66–E79.
- LE BOUTELLER, C. & VENDITTI, J.G. 2014 Vegetation-driven morphodynamic adjustments of a sand bed. *Geophys. Res. Lett.* **41** (11), 3876–3883.
- LIU, C. & NEPF, H. 2016 Sediment deposition within and around a finite patch of model vegetation over a range of channel velocity. *Water Resour. Res.* **52** (1), 600–612.
- LIU, C., SHAN, Y., SUN, W., YAN, C. & YANG, K. 2020 An open channel with an emergent vegetation patch: predicting the longitudinal profiles of velocities based on exponential decay. *J. Hydrol.* **582**, 124429.
- LUHAR, M. & NEPF, H.M. 2016 Wave-induced dynamics of flexible blades. *J. Fluids Struct.* **61**, 20–41.
- MINDERHOUD, P.S.J., COUMOU, L., ERKENS, G., MIDDELKOOP, H. & STOUTHAMER, E. 2019 Mekong delta much lower than previously assumed in sea-level rise impact assessments. *Nat. Commun.* **10** (1), 3847.
- NARAYANA, P.L., TIMBADIYA, P.V. & PATEL, P.L. 2022 Vorticity fields around a pier on rigid and mobile bed channels. *ISH J. Hydraul. Engng* **28** (4), 400–409.
- NITTROUER, J.A., BEST, J.L., BRANTLEY, C., CASH, R.W., CZAPIGA, M., KUMAR, P. & PARKER, G. 2012 Mitigating land loss in coastal louisiana by controlled diversion of mississippi river sand. *Nat. Geosci.* **5** (8), 534–537.
- NORRIS, B.K., MULLARNEY, J.C., BRYAN, K.R. & HENDERSON, S.M. 2021 Relating millimeter-scale turbulence to meter-scale subtidal erosion and accretion across the fringe of a coastal mangrove forest. *Earth Surf. Process. Landf.* **46** (3), 573–592.
- OKHRAVI, S., GOHARI, S., ALEMI, M. & MAIA, R. 2023 Numerical modeling of local scour of non-uniform graded sediment for two arrangements of pile groups. *Intl J. Sedim. Res.* **38** (4), 597–614.
- ORTH, R.J., LEFCHICK, J.S., MCGLATHERY, K.S., AOKI, L., LUCKENBACH, M.W., MOORE, K.A., ORESKA, M.P.J., SNYDER, R., WILCOX, D.J. & LUSK, B. 2020 Restoration of seagrass habitat leads to rapid recovery of coastal ecosystem services. *Sci. Adv.* **6** (41), eabc6434.
- PAOLA, C., TWILLEY, R.R., EDMONDS, D.A., KIM, W., MOHRIG, D., PARKER, G., VIPARELLI, E. & VOLLER, V.R. 2011 Natural processes in delta restoration: application to the Mississippi delta. *Annu. Rev. Mar. Sci.* **3** (2011), 67–91.
- PTASINSKI, P.K., BOERSMA, B.J., NIEUWSTADT, F.T.M., HULSEN, M.A., VAN DEN BRULE, B.H.A.A. & HUNT, J.C.R. 2003 Turbulent channel flow near maximum drag reduction: simulations, experiments and mechanisms. *J. Fluid Mech.* **490**, 251–291.
- ROMINGER, J.T., LIGHTBODY, A.F. & NEPF, H.M. 2010 Effects of added vegetation on sand bar stability and stream hydrodynamics. *J. Hydraul. Engng* **136** (12), 994–1002.
- ROMINGER, J.T. & NEPF, H.M. 2011 Flow adjustment and interior flow associated with a rectangular porous obstruction. *J. Fluid Mech.* **680**, 636–659.
- ROSHKO, A. 1961 Experiments on the flow past a circular cylinder at very high Reynolds number. *J. Fluid Mech.* **10** (3), 345–356.
- SCHEWE, G. 1983 On the force fluctuations acting on a circular cylinder in crossflow from subcritical up to transcritical Reynolds numbers. *J. Fluid Mech.* **133**, 265–285.
- SHAN, Y., ZHAO, T., LIU, C. & NEPF, H. 2020 Turbulence and bed load transport in channels with randomly distributed emergent patches of model vegetation. *Geophys. Res. Lett.* **47** (12), e2020GL087055.

- SIEGERSMA, T.R., WILLEMSSEN, P.W.J.M., HORSTMAN, E.M., HU, Z. & BORSJE, B.W. 2023 Protective structures as adaptive management strategy in nature-based solutions to mitigate sea level rise effects. *Ecol. Engng* **196**, 107079.
- SIEMES, R.W.A., BORSJE, B.W., DAGGENVOORDE, R.J. & HULSCHER, S.J.M.H. 2020 Artificial structures steer morphological development of salt marshes: a model study. *J. Mar. Sci. Engng* **8** (5), 326.
- TANINO, Y. & NEPF, H.M. 2008 Lateral dispersion in random cylinder arrays at high Reynolds number. *J. Fluid Mech.* **600**, 339–371.
- TEMMINK, R.J.M. *et al.* 2022 Recovering wetland biogeomorphic feedbacks to restore the world’s biotic carbon hotspots. *Science* **376** (6593), eabn1479.
- TINOCO, R.O. & COCO, G. 2016 A laboratory study on sediment resuspension within arrays of rigid cylinders. *Adv. Water Resour.* **92**, 1–9.
- TOWNEND, I., FLETCHER, C., KNAPPEN, M. & ROSSINGTON, K. 2011 A review of salt marsh dynamics. *Water Environ. J.* **25** (4), 477–488.
- WELCH, P. 1967 The use of fast fourier transform for the estimation of power spectra: a method based on time averaging over short, modified periodograms. *IEEE Trans. Audio Electroacoust.* **15** (2), 70–73.
- WHITE, B.L. & NEPF, H.M. 2007 Shear instability and coherent structures in shallow flow adjacent to a porous layer. *J. Fluid Mech.* **593**, 1–32.
- WHITE, B.L. & NEPF, H.M. 2008 A vortex-based model of velocity and shear stress in a partially vegetated shallow channel. *Water Resour. Res.* **44** (1), W01412.
- XU, Y., ESPOSITO, C.R., BELTRÁN-BURGOS, M. & NEPF, H.M. 2022 Competing effects of vegetation density on sedimentation in deltaic marshes. *Nat. Commun.* **13** (1), 4641.
- YAGCI, O., YILDIRIM, I., CELIK, M.F., KITSIKOUDIS, V., DURAN, Z. & KIRCA, V.S.O. 2017 Clear water scour around a finite array of cylinders. *Appl. Ocean Res.* **68**, 114–129.
- YAGER, E.M. & SCHMEECKLE, M.W. 2013 The influence of vegetation on turbulence and bed load transport. *J. Geophys. Res.: Earth Surf.* **118** (3), 1585–1601.
- YANG, J.Q., CHUNG, H. & NEPF, H.M. 2016 The onset of sediment transport in vegetated channels predicted by turbulent kinetic energy. *Geophys. Res. Lett.* **43** (21), 11261–11268.
- YANG, J.Q. & NEPF, H.M. 2018 A turbulence-based bed-load transport model for bare and vegetated channels. *Geophys. Res. Lett.* **45** (19), 10428–10436.
- YI, Z., SUN, Y., WANG, X., LIU, D. & YAN, X. 2021 Numerical analysis of hydrodynamics influenced by a deformed bed due to a near-bank vegetation patch. *Water Suppl.* **22** (2), 1546–1556.
- ZHANG, Y., JEPPESEN, E., LIU, X., QIN, B., SHI, K., ZHOU, Y., THOMAZ, S.M. & DENG, J. 2017 Global loss of aquatic vegetation in lakes. *Earth-Sci. Rev.* **173**, 259–265.
- ZHANG, Y.-H., DUAN, H.-F., YAN, X.-F. & STOCCHINO, A. 2023 Experimental study on the combined effects of patch density and elongation on wake structure behind a rectangular porous patch. *J. Fluid Mech.* **959**, A36.
- ZHAO, T. & NEPF, H.M. 2021 Turbulence dictates bedload transport in vegetated channels without dependence on stem diameter and arrangement. *Geophys. Res. Lett.* **48** (21), e2021GL095316.
- ZONG, L. & NEPF, H. 2011 Spatial distribution of deposition within a patch of vegetation. *Water Resour. Res.* **47** (3), W03516.
- ZONG, L. & NEPF, H. 2012 Vortex development behind a finite porous obstruction in a channel. *J. Fluid Mech.* **691**, 368–391.